

An Electro-thermal De-icing Model and Simulation Analysis Considering Ice Shedding

ZHANG Yingying¹, YUAN Xiansheng², XIONG Jingjiang², BU Xueqin^{1*}

1. School of Aeronautic Science and Engineering, Beihang University, Beijing 100191, P. R. China;

2. AECC Hunan Aviation Powerplant Research Institute, Zhuzhou 412002, P. R. China

(Received 15 January 2025; revised 1 March 2025; accepted 2 March 2025)

Abstract: The electro-thermal anti/de-icing systems have high heating efficiency and relatively simple structures, marking them as a key development direction for future icing protection. Existing simulation algorithms for electro-thermal de-icing seldom delve into comprehensive ice accretion-melting-deicing models that account for ice shedding. Therefore, the detachment behavior of ice layers during the heating process requires in-depth research and discussion. This paper physically models the phenomenon of ice shedding, incorporates the detachment behavior of ice layers during heating, improves the existing mathematical model for electro-thermal de-icing calculations, establishes an ice accretion-melting-deicing model for electro-thermal de-icing systems, and conducts numerical simulation, verification and optimization analysis of electro-thermal de-icing considering ice shedding. Through multi-condition de-icing numerical simulations of a specific wing model, it is found that ambient temperature can serve as a factor for adapting the electro heating anti/de-icing strategy to the environment. An optimization of heating heat flux density and heating/cooling time is conducted for the wing de-icing control law under the calculated conditions. The improved electro-thermal de-icing model and algorithm developed in this paper provide solid technical support for the design of electro-thermal de-icing systems.

Key words: aircraft icing; electro-thermal de-icing; ice shedding; electro-thermal control law; numerical simulation

CLC number: V244.1

Document code: A

Article ID: 1005-1120(2025)02-0162-16

0 Introduction

Aircraft icing occurs when an aircraft is flying under icing conditions due to the freezing of water droplets, condensation of water vapour or adhesion of ice crystals, which can accumulate on the aircraft surface to form an ice layer. Aircraft icing not only increases the mass, but may also lead to aerodynamic performance degradation, air intake blockage, and even loss of aircraft control, seriously endangering flight safety. Among all icing phenomena, super-cooled water droplets icing is the main target of aircraft icing and protection research.

With the in-depth study of large passenger aircraft, in order to meet the higher requirements of airworthiness certification for flight safety under ic-

ing conditions, aircraft anti/de-icing systems are designed to reduce energy consumption and ensure anti/de-icing effectiveness, and are developing towards economic, green and more electric aircraft. Among many methods of anti-icing and de-icing, electro-thermal anti/de-icing system has features of high heating efficiency, short response time, high reliability, relatively simple structure, and being easy to control and monitor, so it has become an important development direction for wide range of composite materials. The working process of electro-thermal anti/de-icing system is a complex unsteady multiphase flow and phase change problem, which involves external air-water droplet two-phase flow, runback water film flow on the surface,

*Corresponding author, E-mail address: buxueqin@buaa.edu.cn.

How to cite this article: ZHANG Yingying, YUAN Xiansheng, XIONG Jingjiang, et al. An electro-thermal de-icing model and simulation analysis considering ice shedding [J]. Transactions of Nanjing University of Aeronautics and Astronautics, 2025, 42(2): 162-177.

<http://dx.doi.org/10.16356/j.1005-1120.2025.02.002>

phase changes between solid ice and liquid water, heat transfer in the ice layer with varying thickness, and unsteady internal heat conduction in the multi-layered skin^[1]. Simulation is a necessary and important tool in the design study.

From the 1970s to the present, the research on electro-thermal de-icing has gone through the development of 1D ice melting model-2D ice melting model-3D ice melting model-flight state de-icing model. Chauvin et al.^[2] investigated the heat transfer in skins during icing. The first numerical simulation of unsteady ice accretion-melting-deicing process was carried out by Reid et al.^[3] in 2010. Based on the above studies, Pourbagian et al.^[4] conducted an optimization study of electro-thermal de-icing process in 2013 and deepened the optimization in 2015^[5]. The work of Henry^[6] demonstrated the importance of melting ice for ice shedding phenomenon of electro-thermal de-icing systems, defining an empirical ice shedding criterion and comparing it with experimental data from the CEPr icing wind tunnel. Bennani et al.^[7] proposed a research to simulate the operation of the electro-thermal system in anti-icing and de-icing modes by using thermodynamic and crack extension mechanics models in conjunction with the above mentioned empirical guidelines and compared them with experimental results. In 2020 Ding et al.^[8] proposed that during electro-thermal de-icing, before the phase change of the icing on an aircraft surface occurs, the stresses in the ice layer may have an effect on ice shedding. Kintea et al.^[9] investigated the phenomenon of aircraft icing and ice shedding due to ice crystal impacts, which was solved numerically using a computational code based on the finite volume method (FVM). Numerous research units have conducted studies on ice shedding for rotorcraft in recent years. They have presented numerical predictions for ice accretion and break-off, shedding times, and icing wind tunnel tests on the spinning rotor blade model for assessment^[10-12]. Subsequently, experimental tests in icing wind tunnel of airfoil equipped with a de-icing system were carried out to investigate the ice shedding

times. The results of Wallisch et al.^[13] showed that the angle of attack influences the shedding times significantly. Enache et al.^[14] obtained several ice shedding mechanisms highlighting the effect of the water layer thickness on the ice shedding process.

Meanwhile, various research institutes have developed electro-thermal de-icing simulation software or modules, for example, NASA has developed the LEWICE program^[15-16], and NTI has developed the FENSAP-ICE software with an electro-thermal de-icing calculation module^[17-18]. ONERA software^[19] includes a calculation function that analyses the process of 2D electro-thermal de-icing using the finite element method (FEM).

Practical engineering challenges are the primary focus of domestic research on electro-thermal de-icing systems. Ai et al.^[20] proposed the idea of applying electro-thermal de-icing system to helicopter rotor blades. Bu et al.^[21] calculated the convective heat transfer coefficient on the surface of electro-thermal anti-icing system using the boundary layer integral method, and established a heat and mass transfer model to solve the temperature distribution on the surface. Chang et al.^[22] established a physically simplified model of a 2D rectangular geometry to simulate the electro-thermal de-icing system. Li^[23] carried out a simulation of helicopter rotor electro-thermal de-icing system based on Fluent platform, solved the melting ice process by using the enthalpy method, and analyzed the influence of the control law on the de-icing effect. Fu et al.^[24] analyzed the 2D electro-thermal de-icing process based on Messinger model with improved enthalpy method, whose ice shape was calculated using numerical simulation method, and analyzed the melting ice process on results of ice accretion calculations. They analyzed the influence of the control law of the heating time and the heat flux on the temperature. Mu^[25] carried out a study on the 3D electro-thermal de-icing process in flight, established a unsteady coupled heat transfer model for the de-icing process, and proposed a corresponding solution method.

However, the above electro-thermal de-icing models have explored less about the ice shedding

phenomenon, which occurs during the actual de-icing process and needs to be taken into account in the de-icing models and simulations. In this paper, through reading related literatures, we model the phenomenon of ice shedding, introduce the shedding behavior of ice in the heating process, improve the existing numerical calculation model of electro-thermal de-icing, establish a complete ice accretion-melting-deicing model for electro-thermal de-icing systems, and carry out numerical calculation of electro-thermal de-icing considering ice shedding. Through multi-condition de-icing numerical simulations, the influence of parameters on the effect of electro-thermal de-icing is analyzed, and the design method of electro-thermal de-icing considering ice shedding is summarized, so as to provide a theoretical basis in reducing the energy consumption of electro-thermal de-icing.

1 Calculation Models

The working process of electro-thermal de-icing system is a complex unsteady multiphase flow and phase change problem, coupled with heat and mass transfer, the physical phenomena of which can be shown in Fig.1. Runback water film flows on the surface and phase change with ice shedding occurs under the influence of external convective heat transfer, supercooled water droplet impingement, and structural heating. In this chapter, the airflow field and particle motion model, icing thermodynamic model, and ice shedding model are introduced.

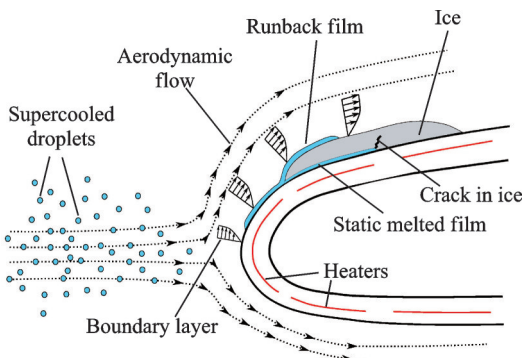


Fig.1 Schematic diagram of physical phenomena in electro-thermal de-icing system

1.1 Airflow field and water droplet motion model

The airflow field calculation is a necessary prerequisite for the prediction of droplet impingement characteristics. The results can be used for calculations of droplet trajectories, external convective heat transfer and de-icing analysis. The airflow field is formulated using the Reynolds-averaged Navier-Stokes (RANS) equations, and the Reynolds stress term is defined by the Boussinesq assumption as

$$\frac{\partial \rho}{\partial t} + \frac{\partial (\rho u_i)}{\partial x_i} = 0 \quad (1)$$

$$\frac{\partial}{\partial t} (\rho u_i) + \frac{\partial}{\partial x_j} (\rho u_i u_j) = -\frac{\partial p}{\partial x_i} + \frac{\partial}{\partial x_j} \left[\mu \left(\frac{\partial u_i}{\partial x_j} + \frac{\partial u_j}{\partial x_i} - \frac{2}{3} \delta_{ij} \frac{\partial u_l}{\partial x_l} \right) \right] + \frac{\partial}{\partial x_j} (-\rho \overline{u'_i u'_j}) \quad (2)$$

$$-\rho \overline{u'_i u'_j} = \mu_t \left(\frac{\partial u_i}{\partial x_j} + \frac{\partial u_j}{\partial x_i} \right) - \frac{2}{3} \left(\rho k + \mu_t \frac{\partial u_k}{\partial x_k} \right) \delta_{ij} \quad (3)$$

where u is the Reynolds average velocity vector, ρ the air density, μ the dynamic viscosity, μ_t the turbulent viscosity, and k the turbulent energy.

After calculating the results of the airflow field, the droplet impingement characteristics are calculated using Euler method. The Eulerian method treats the water droplet phase as a continuous phase and solves the continuity and momentum equations for the droplet field by introducing the concept of water droplet volume fraction, which can be shown as

$$\frac{\partial (\rho_d \alpha)}{\partial t} + \nabla \cdot (\rho_d \alpha \mathbf{u}_d) = 0 \quad (4)$$

$$\frac{\partial (\rho_d \alpha \mathbf{u}_d)}{\partial t} + \nabla \cdot (\rho_d \alpha \mathbf{u}_d \mathbf{u}_d) = \rho_d \alpha K (\mathbf{u}_a - \mathbf{u}_d) + \rho_d \alpha F \quad (5)$$

where α is the water droplet volume fraction, \mathbf{u}_d the water droplet velocity vector, \mathbf{u}_a the air velocity vector, F the external force other than drag acting on the water droplet, and K the air-water droplet momentum exchange coefficient. Here K is defined as

$$K = \frac{18\mu f}{\rho_d d_d^2} \quad (6)$$

where d_d is the droplet diameter, and f the drag function. Here f is calculated as

$$f = \frac{C_D Re}{24} \quad (7)$$

$$C_D = \begin{cases} 24(1 + 0.15Re^{0.687})/Re & Re \leq 1000 \\ 0.44 & Re > 1000 \end{cases} \quad (8)$$

where C_D is the droplet drag coefficient, and Re the relative Reynolds number.

The droplet velocity vector \mathbf{u} , volume fraction α and other results are obtained from the calculation of the droplet field, and further the droplet impingement mass on the impact surface can be obtained as

$$\dot{m}_{imp} = \rho_d \alpha \mathbf{u} \cdot \mathbf{n} \quad (9)$$

where \mathbf{n} is unit vector in the normal direction.

1.2 Icing thermodynamic model

The icing thermodynamic model is based on the Messinger's theory. The model uses the control volume method to analyse the mass transfer and energy transfer processes in the liquid water control volume at the wall. The mass and energy transfer processes involved in the control volume is schematically illustrated in Fig.2. The calculations start from the stagnation point and are finalised for the full computational domain by analytically calculating the conservation of mass and conservation of energy in the control units.

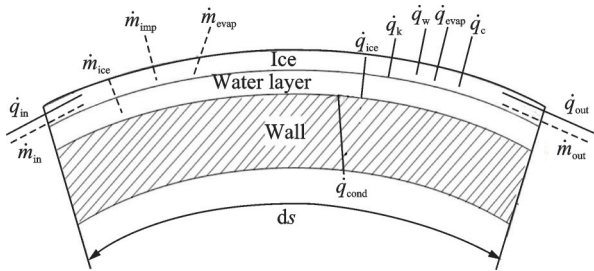


Fig.2 Mass and energy transfer processes of control volume

The mass conservation equation is expressed as

$$\dot{m}_{ice} = \dot{m}_{imp} + \dot{m}_{in} - \dot{m}_{evap} - \dot{m}_{out} \quad (10)$$

where \dot{m}_{imp} is the mass flow rate of water impinging on the control volume, \dot{m}_{evap} the mass flow rate of evaporation water, and \dot{m}_{ice} the mass flow rate of water frozen to ice; \dot{m}_{in} and \dot{m}_{out} are the inflow/outflow mass flow rates of the control volume, respectively.

The energy conservation equation is expressed as

$$\dot{q}_{in} + \dot{q}_{ice} + \dot{q}_{cond} + \dot{q}_k = \dot{q}_{out} + \dot{q}_{evap} + \dot{q}_c + \dot{q}_w \quad (11)$$

where \dot{q}_k is the kinetic energy of supercooled water droplets impinging on the control volume, \dot{q}_{evap} the latent heat of water evaporation on the surface, \dot{q}_{ice} the latent heat of water freezing, \dot{q}_{cond} the heat flux of the electro-thermal de-icing system transferred to the surface through the skin conduction, \dot{q}_w the heat flux of heating water, \dot{q}_c the heat flux of the convective heat exchange, \dot{q}_{in} the sensible heat of water from the previous control volume, and \dot{q}_{out} the sensible heat of water exiting the control volume.

When water droplets impinge on the wall, they partially evaporate within the heating zone, partially flow along the surface in the direction of the air flow, and partially freeze within the computational domain. The computational domain is divided into three scenarios for consideration: temperatures above, equal to, and below the freezing point. (1) Above the freezing point, the wall may be a dry surface above 0 °C (273.15 K) or a wet surface with liquid water but no ice; (2) equal to the freezing point, there may be both runback water and freezing ice on the surface simultaneously, or it may be a dry surface with the temperature of 0 °C (273.15 K); (3) below the freezing point, it can either be a dry surface below 0 °C (273.15 K) or an icing region where all surface water has frozen into ice, but thermal equilibrium cannot be maintained, causing the surface temperature to further decrease. The freezing factor f is the ratio of the mass flow rate of frozen ice to the total volume of water on the de-icing surface, shown as

$$f = \frac{\dot{m}_{ice}}{\dot{m}_{in} + \dot{m}_{imp}} \quad (12)$$

By performing calculations on the computational domain based on different freezing coefficients, computational efficiency can be improved.

1.3 Ice shedding model

The phenomenon of ice shedding from the surface during the electro-thermal de-icing process is primarily governed by the air shear force and the adhesive force of the ice^[26]. Since ice tends to shed in patches during actual de-icing, the influence of ice cohesion force is neglected in the current study. The air shear force is the resultant force exerted by the

airflow field on the ice surface, and the impact of the ice surface must be considered. The adhesive force refers to the bonding force between the ice and the surface, which is related to factors such as the structural state of the ice and the ambient temperature. As shown in Fig.3, the ice shedding criterion is combined with the empirical criterion and the physical criterion. The latter item judges the relative magnitude of the air shear force F_τ and the adhesion force $F_{adhesion}$ of the icing area. If $F_\tau > F_{adhesion}$, then ice on the area is shedding.

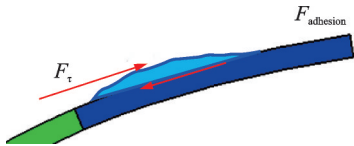


Fig.3 Diagram of ice shedding criterion

Experimental measurements of ice adhesion stress are related to a variety of factors such as experimental conditions and measurement methods, with a wide range of variations. A summary of current studies in literatures related to the magnitude of adhesion stresses on different materials for icing surface is shown in Table 1.

Table 1 Summary of literatures about adhesion stress

Literature	Ice type	Substrate material	Adhesion stress/MPa
Rønneberg et al. ^[27]	Impact ice	Aluminium	0.21—0.76
Fu et al. ^[28]	Frozen water	Titanium, aluminium, graphene coating, brass	0.03—0.51
Scavuzzo et al. ^[29]	Artificial ice	Aluminium, stainless steels	0.27—0.54
Laforte et al. ^[30]	Rime and glaze	Aluminium	0.07—0.40

Currently, the simulation calculations use the adhesion data measured by Fu^[28] on an aluminum alloy surface, with a range of 0.449—0.621 MPa. The average value of eight experimental records, 0.492 MPa, is adopted.

Due to the complex physical mechanisms of ice adhesion, ONERA initially used an empirical ice shedding criterion in icing and anti/de-icing simula-

tion calculations. This empirical model makes the following assumption, as shown in Fig.4. If the ratio of the water film length to the total ice length, L_f/L_t , exceeds a user-defined threshold (recommended value is 80%), the ice will detach from the structure. Specific parameters can be adjusted based on correlation with experimental data, and this paper adopts 80%. The implementation of this empirical criterion is relatively simple, which is used as the method in the research.

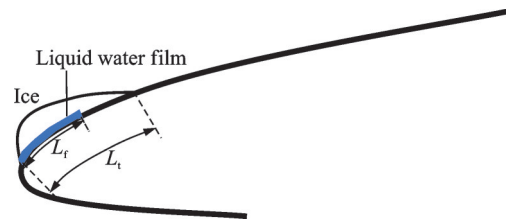


Fig.4 Diagram of ice shedding empirical model

To summarize this section, the ice shedding criterion can be expressed as

$$\text{Ice-Shedding} = \begin{cases} F_\tau > F_{adhesion} & \text{Physical model} \\ L_f/L_t > 80\% & \text{Empirical model} \end{cases} \quad (13)$$

By integrating the air shear force and adhesive force within each heating zone, the relative magnitudes of the air shear force and ice adhesive force in the zone are evaluated. Combined with the empirical shedding criterion, if either of the two conditions in Eq.(13) is satisfied, the ice in that zone will detach. This establishes a model for the physical phenomenon of ice shedding during the electro-thermal de-icing process, laying the foundation for subsequent simulation calculations.

2 Calculation Methods

The electro-thermal de-icing calculation methods primarily include computations of the airflow field, water droplet impingement characteristics, surface overflow phase change, and structural heat conduction. The calculation procedure is illustrated in Fig.5. The two-phase flow field, the runback water film flow on the surface, phase changes between solid ice and liquid water, and structural heat conduction are coupled. The water droplet flow field de-

depends on the distribution of the airflow field, while the calculation of structural heat conduction provides heating heat flux data for the runback water film overflow and phase changes. Simultaneously, its thermal boundary conditions are determined by the overflow and phase change state, requiring coupled solutions^[31]. Considering that the ice thickness during the de-icing process is very thin and the ice accretion has minimal influence on the external flow, the model neglects changes in the external flow field during de-icing to reduce computational costs and accelerate calculation speed. The calculations are based on steady-state flow field results, and one-way coupling is performed.

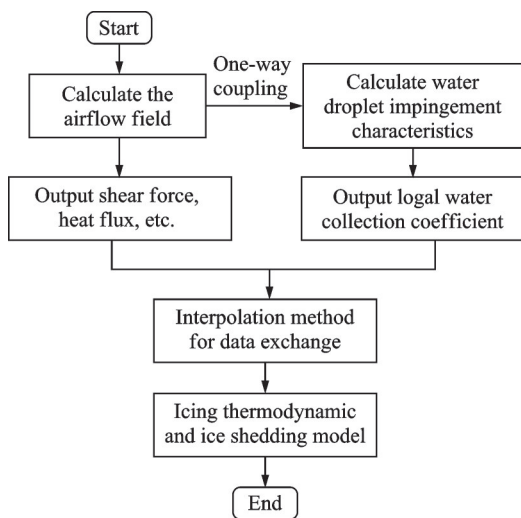


Fig.5 Flow chart of simulation

The steady state solution of the external air-droplet flow field is calculated as an input to the internal icing thermodynamic calculations, and data are exchanged using interpolation for unsteady state de-icing simulations due to the difference between flow field mesh and solid mesh and coupled to solve the structural thermal conductivity and icing thermodynamic by exchanging boundary conditions.

The airflow field simulation is based on the FLUENT software. The droplet impingement characteristics are solved using Eulerian method and the control equations are discretised using the finite volume method and solved in second order windward format. The solution process of equations utilises the user defined scalar (UDS) transport equations

provided by the FLUENT software solver. The air-water droplet flow field data acts as input for icing thermodynamic and structural heat conduction. To address the mismatch between the external flow field grid and the structural grid of the protected region, an inverse distance squared interpolation method is employed for data mapping, enabling the acquisition of physical quantity distributions on the protected surface.

The heat conduction in the structure and the phase transition process are solved using a loosely coupled method^[32]. The Dirichlet heat boundary condition of heat conduction is provided on the outer surface of the wall by the temperature results of the solution of water film runback and phase transition during the coupled solution. In return, the de-icing heat flux on the outer surface is calculated by solid heat conduction simulation and sent as the heat-flux boundary for the calculation of water film overflow and phase transition. At the current time step, both the solid heat conduction and the phase transition on the surface (including ice accretion, melting, and de-icing) are iteratively calculated until convergence. During the iteration process, the iterative calculations within the current time step are advanced by continuously updating the surface temperature and heat flux boundary conditions. The specific steps of the coupled solution are as follows:

Step 1 Loop through all surface control volumes. If the mass flow rate entering the control volume is known, it is considered that the initial state of the control volume is known. The mass and energy conservation equations for the overflow water of the control volume are calculated to obtain the mass flow rate exiting the control volume (which is also the mass flow rate entering the adjacent control volume) and the temperature result of the control volume. If it is unknown, the calculation of the control volume is skipped. By repeatedly searching for the state of the control volumes, the overflow water flow results and surface temperature results of all control volumes can be iteratively calculated, thereby obtaining the temperature distribution of the sur-

face.

Step 2 Using the calculation results from Step 1 to provide Dirichlet boundary condition for solid heat conduction in the structure, calculate the temperature distribution inside the structure and the heat flux at outside boundary.

Step 3 Using the calculation results from Step 2 to update the heating heat flux of the surface control volumes, repeat Steps 1 and 2 until the calculations within the current time step converge.

Step 4 Update the surface condition and proceed to the next time Step calculation.

For the judgement of ice shedding during iteration, the procedure is shown in Fig.6.

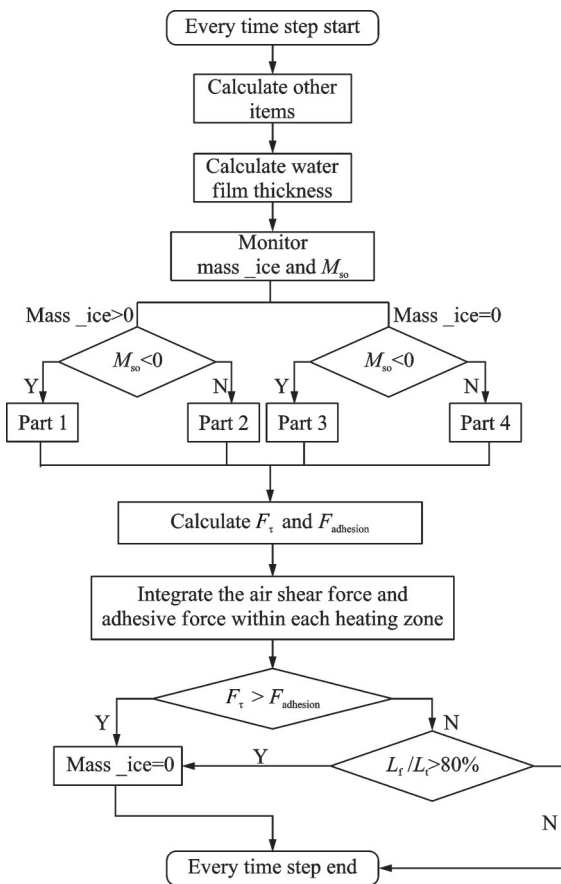


Fig.6 Flow chart of ice shedding procedure

In the simulation, after the calculations converge within each time step, we monitor the mass of ice accretion in the control volume ($mass_ice$) and the ice accretion/melting rate (M_{so}) to compute the ice thickness and water film thickness. These two physical quantities, $mass_ice$ and M_{so} , can be

used to discuss and partition the wall regions. By dividing the wall into zones, different states of the wall surface at each time step can be visually represented, facilitating subsequent integral calculations of ice adhesion forces. Specifically, when $mass_ice > 0$, $M_{so} \geq 0$, ice is accumulated on the surface, and the ice protection surface experiences water freezing, denoted as Part 2. In this case, the ice adhesion force model needs to be calculated. The air shear force and adhesion force data for each grid on the wall are obtained through calculations. By looping the wall grids, the air shear force and adhesion force within each heating zone are integrated, while the water film conditions in each heating zone are recorded. Finally, ice shedding is determined by comparing the relative magnitudes of the air shear force and ice adhesion force within the zone, as well as the ratio of the water film length to the ice length. If the shedding criterion is met, the ice mass in the grid is reset to zero, thereby simulating the phenomenon of ice shedding.

3 Calculation Results and Analysis

3.1 Validation of calculation models

To validate the unsteady de-icing calculation models, we refer to experimental data from the NASA Lewis Icing Wind Tunnel on electro-thermal de-icing experiment conducted by Al-Khalilk et al.^[33]. Experimental wing section profile is NACA0012 with a chord length of 0.914 4 m. The atmospheric and icing conditions of Al-Khalilk's experiment are listed in Table 2. The leading edge consists of a layup composite in which seven heater pads are implemented as ice protection system. The material properties of each layer in the ice protection area are provided in Table 3. The positions of heaters on the leading edge is shown in Fig.7. The heating control law used in the experiment is illustrated in Fig.8, with the heater power density set as heater A at 7 750 W/m², heaters B and C at 15 500 W/m², and heaters D, E, F, and G at 12 400 W/m².

Table 2 Experimental environmental conditions for Al-Khalilk's experiment

Temperature $t_{\infty}/^{\circ}\text{C}$	AOA/ $(^{\circ})$	Velocity $V_{\infty}/(\text{m}\cdot\text{s}^{-1})$	MVD/ μm	LWC/ $(\text{g}\cdot\text{m}^{-3})$
-6.67	0	44.7	20	0.78

Table 3 Physical properties of materials in Al-Khalilk's experiment

Material	Thickness/mm	Density $\rho/(\text{kg}\cdot\text{m}^{-3})$	$C_p/(\text{J}\cdot\text{kg}^{-1}\cdot^{\circ}\text{C}^{-1})$	$k/(\text{W}\cdot\text{m}^{-1}\cdot^{\circ}\text{C}^{-1})$
Erosion shield	0.2	8 025.25	502.4	16.26
Elastomer	0.56	1 383.96	1 256.0	0.256 1
Fiberglass	0.89	1 794	1 570.1	0.294
Silicon foam insulation	3.4	648.75	1 130.4	0.121

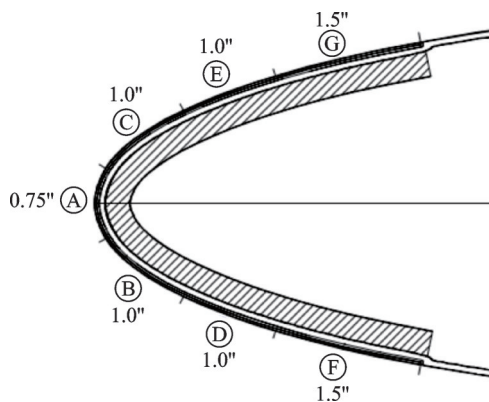


Fig.7 Schematic diagram of validation model

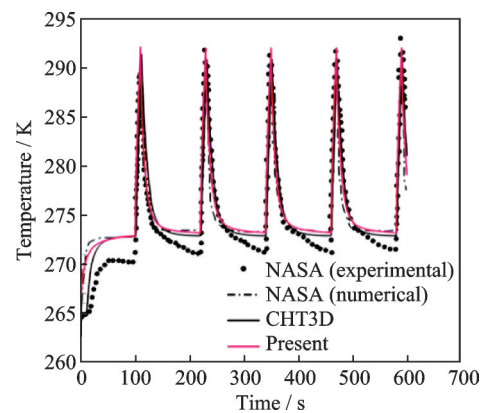


Fig.9 Temperature rise curves

The deicing cycle (120 s)			
Heater G			10
Heater E			10
Heater C		10	
Heater A	100		
Heater B		10	
Heater D			10
Heater F			10
Time	100	110	120

Fig.8 Schematic diagram of Al-Khalilk's experimental heating control law

The unsteady de-icing models considering ice shedding are solved as described above. Fig.9 shows the temperature variation over time at the location of heater B. There is no significant ice shedding phenomenon observed during the calculation. The computation results are compared with experimental data from the literature, showing similar temperature trends with temperature difference within 6 K, which confirms the correctness of the proposed model and calculation methods.

The simulated temperature results are slightly higher than the experimental data. The main deviation lies in the temperature plateau during the cooling phase. This study employs the icing thermodynamic model that sets the temperature of the surface

ice-water mixed state as the freezing point temperature, without accounting for supercooled runback water overflow phenomenon. If phenomenon exists, the structural temperature may drop below the phase-transition temperature.

3.2 Calculation object and conditions

The model used in the simulation is a 2D airfoil structure with a chord length of 0.58 m. The heating pads are installed on the leading edge of the airfoil using a bonding method, as shown in Fig.10. The heating zone is located on the upper surface of the airfoil model with an arc length of 88 mm and on the lower surface with an arc length of 122 mm. The computational domain for the air flow field has a radius of 10 m to ensure the pressure far field boundary and the flow field mesh is a structured mesh with 34 080 grids. The y^+ at the ice protection area of the mesh file is controlled lower than 1. The solid mesh with 4 845 grids is chosen for heat transfer calculations. The time step is set to 1 s, which is computationally efficient and can improve convergence outcomes.

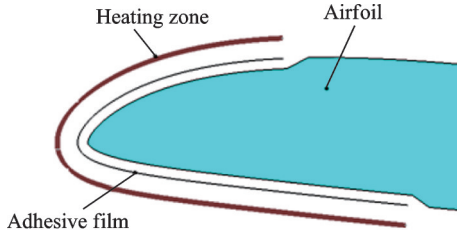
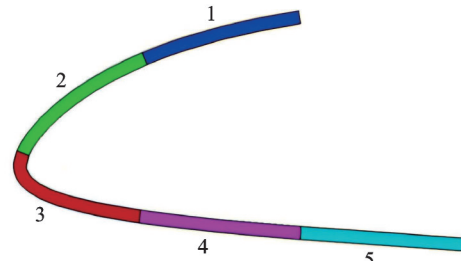


Fig.10 Schematic diagram of heating component installation

The leading edge consists of a 5-layer composite structure in which five heater pads are implemented as ice protection system. Physical property parameters of each layer of the model are shown in Table 4.

The heating assembly adopts a de-icing method, dividing the protected area equally into five heating zones along the chord. Only one zone (one heater) operates at a time, with the zones and heating control law 1 shown in Fig.11.

Calculation conditions of the 2D airfoil are



(a) Schematic diagram of heating zones

Heating control law 1 (127 s)											
Heater 1										5	
Heater 2	4				4						
Heater 3		5				5					
Heater 4			4				4				
Heater 5										5	
Turn off				36				31			24
	4	9	13	49	53	58	62	93	98	103	127

(b) Schematic diagram of heating control law 1

Fig.11 Schematic diagrams of heating zones and heating control law 1

shown in Table 5. In Cases 1—3, all heaters set power density are 4 W/cm^2 , and Cases 2, 3 changed the ambient temperature for calculation.

Table 4 Physical properties of materials in present experiment

Designation	Thickness/mm	Density $\rho/(\text{kg}\cdot\text{m}^{-3})$	$c_p/(\text{J}\cdot\text{kg}^{-1}\cdot\text{C}^{-1})$	$k/(\text{W}\cdot\text{m}^{-1}\cdot\text{C}^{-1})$
Leading edge sheath	0.5	7 800	502	16.7
Insulation	0.1	1 400	1 200	0.2
Insulation + adhesive film	0.2	1 250	1 300	0.32
Fiberglass	0.39	1 730	1 050	0.26
Carbon fiber	2.13	1 450	1 080	0.43

Table 5 Calculation conditions

Case	Pressure/Pa	AOA/(°)	$V_\infty/(\text{m}\cdot\text{s}^{-1})$	t_∞/C	MVD/ μm	LWC/ $(\text{g}\cdot\text{m}^{-3})$	Control law
1	57 208	1.11	178.84	-10	25	0.3	1
2	57 208	1.11	178.84	-20	25	0.3	1
3	57 208	1.11	178.84	-5	25	0.3	1

3.3 Analysis of ice shedding calculation results

The analysis is conducted on a specific time period during the heating cycle of Heater 1 in Case 1, where ice shedding is observed and easily detectable.

As shown in Fig.12, by comparing scatter plots of ice thickness versus the y -coordinate at different times, it is found that at 94 s, after a period of icing, the ice shapes calculated using the ice shedding model and the no-shedding model are largely consistent. At 95 s, ice shedding occurs. At this point, Heater 1 is active, and the structural heat transfer causes the ice in this region to melt and

shed, which is a reasonable result. After 95 s, the ice accretion continues to be calculated until the end of the heating cycle at 127 s. With incorporating the ice shedding model, the ice mass on the airfoil decreases by 37% at 95 s (assuming an ice density of 917 kg/m^3). By the end of the calculation at 127 s, the ice mass on the airfoil decreases by 28%, demonstrating the importance of the ice shedding model in predicting de-icing time and studying efficient electro-thermal de-icing strategies.

For Heater 2 in Case 1, the ice thickness and temperature data are taken from the calculation results at the center of each heater. As shown in

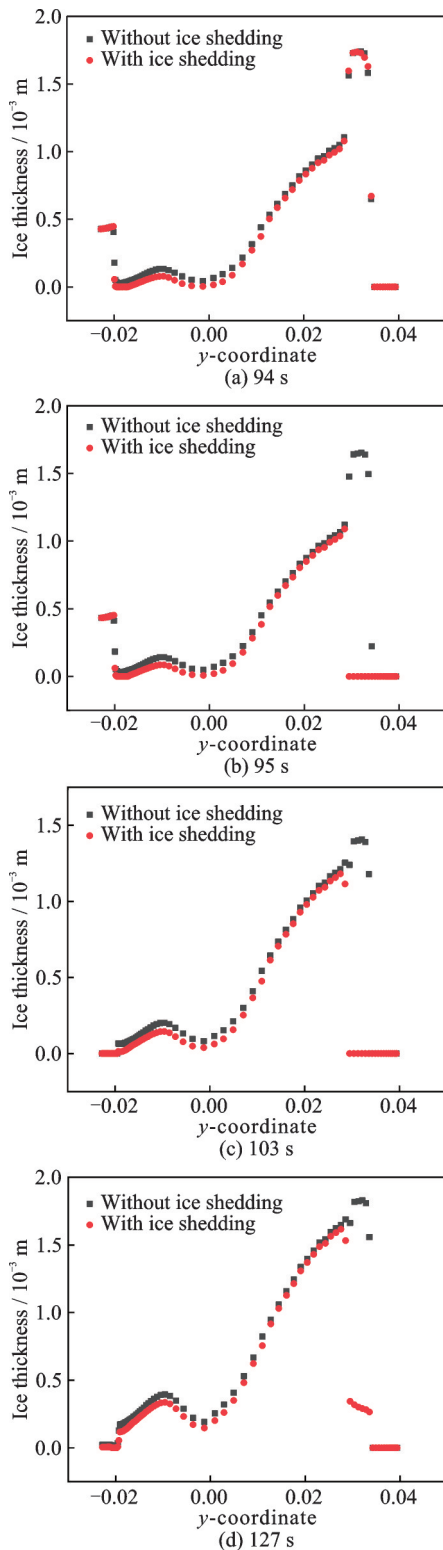


Fig.12 Comparison of ice thickness on Heater 1 in Case 1

Fig.13, plots of ice thickness, surface temperature, and heater power density versus time are presented.

The maximum ice thickness at the location of Heater 2 is 0.105 4 cm at 127 s, and the highest temperature is 278.3 K at 4 s. Heater 2 is active from 0 to 4 s, during which there is no ice accretion

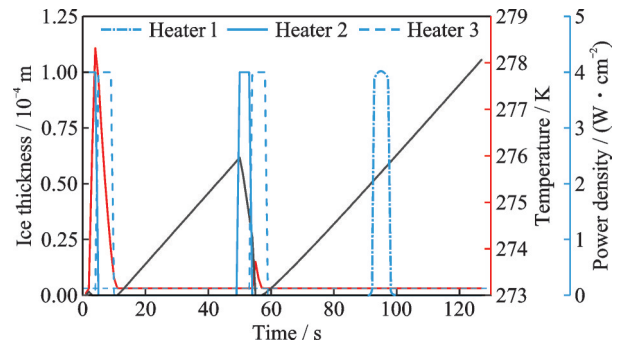


Fig.13 Simulation calculation results for Heater 2 in Case 1

on the surface, and the wall temperature quickly rises above the freezing point. After 4 s, Heater 2 is turned off, and the wall temperature decreases. The rise in wall temperature is primarily due to the activation of the heating pad at this location, with almost no influence from adjacent heating pads. After 4 s, when the wall temperature drops to the freezing point, the surface enters a two-phase state of icing, and ice begins to accumulate, increasing in the thickness. However, the skin temperature remains at the freezing point and does not drop below 0 °C, preventing more severe ice accretion. After a period of icing, Heater 2 operates again from 53 s to 57 s, initiating de-icing. The calculation data show that the wall temperature remains at 0 °C for a period, indicating a two-phase state of melting ice. In the final second of this heater's operation, the ice at this location is completely removed, and the temperature rises above 0 °C. Simultaneously, ice shedding is observed in the plot. Ice shedding occurs when the heater is working to melt ice, which is a reasonable result. After 57 s, the wall temperature quickly drops to 0 °C, and ice accretion begins again.

The calculation results for Heaters 3 and 4 in Case 1 are similar to those of Heater 2, with the difference being that due to the lower water impingement compared to Heater 2, the ice thickness is smaller, and the ice is quickly removed when heaters are activated for the second time, causing the skin temperature to rise above 0 °C rapidly. The area where Heater 1 is located is the overflow zone, primarily influenced by the runback water formed after Heater 2 is activated. The ice thickness here is relatively thin, and the ice can be removed after heating begins at 98 s.

The de-icing strategy is relatively reasonable, with the surface temperature exceeding $0\text{ }^{\circ}\text{C}$ for a short duration and the maximum temperature not being excessively high. This ensures the effectiveness of electro-thermal de-icing while maintaining low energy consumption. Due to the thin ice accumulation during the icing cycles, the ice can be removed quickly.

For Heater 5 in Case 1, as shown in Fig.14, Heater 5 is activated from 98 s to 103 s. Before the heating pad is activated, due to the low water impingement at the location of Heater 5, the wall temperature remains at the freezing point, and the surface is in a two-phase state of icing, leading to an increase in ice thickness. However, the wall temperature remains at the freezing point and does not drop below $0\text{ }^{\circ}\text{C}$, preventing more severe ice accretion. After Heater 5 is activated at 98 s, due to the thin ice layer, the wall temperature initially remains at $0\text{ }^{\circ}\text{C}$, with the surface in a two-phase state of melting ice (solid ice and liquid water coexistence). The ice is then completely removed, and the temperature rises above $0\text{ }^{\circ}\text{C}$, reaching its peak. After the heating pad stops operating, the wall temperature gradually decreases. By the end of the calculation at 127 s, the temperature remains above $0\text{ }^{\circ}\text{C}$, and there is no ice accretion on the surface.

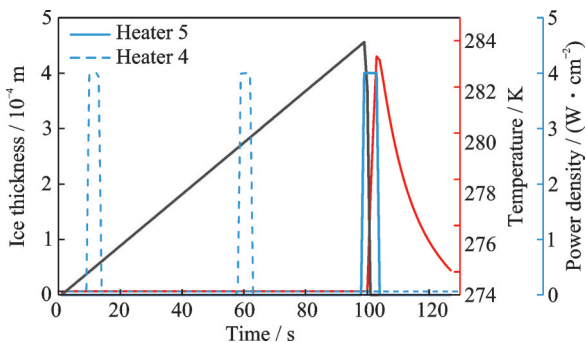


Fig.14 Simulation calculation results for Heater 5 in Case 1

For Case 1, the de-icing strategy is relatively reasonable, with the maximum temperature not being excessively high. However, due to the low water impingement at this location, the ice accretion rate is slow, and the ice layer is thin, allowing the ice to be removed quickly. While ensuring the effectiveness of electro-thermal de-icing, energy con-

sumption can be reduced by decreasing the heat flux of the heating pads.

4 Influencing Factors on De-icing Effect and Optimization of Heating Control Law

4.1 Influence of ambient temperature on de-icing effect

The analysis on three different temperature conditions of heating zone 2 is illustrated in Fig.15. The simulation time is plotted on the x -axis, while the ice thickness and surface temperature are plotted on the y -axis in a line graph. Under the same electro-thermal control law, the ambient temperature has a significant influence on the surface temperature and ice accretion.

Heater 2 is the location where the maximum ice thickness occurs. In Fig.15(a), under the condition of an ambient temperature of $-20\text{ }^{\circ}\text{C}$, the ice is not completely removed, whereas the other two conditions effectively remove the ice at the heating control law 1. Further analysis reveals that the lower the ambient temperature, the higher the ice accretion rate, and the longer the de-icing time required. In Fig.15(b), within the time range of the first working time of Heater 2, the higher the ambient temperature, the greater the surface temperature rise. During the second working time of Heater 2 between 53—57 s, the curves show significant differences. In Case 3, since the surface temperature does not drop to the freezing point before the second heating begins, the surface temperature rapidly rises to a higher level, resulting in unnecessary energy consumption. In Case 2, since the ice is not completely removed, the surface temperature remains at the freezing point for melting. And then with both water and ice on the surface, the wall is in the phase change state of ice accretion. In the calculation, when the ambient temperature is lower than the design condition, the heating control law can be adjusted by monitoring the ice thickness to ensure that the ice thickness does not exceed the allowable value during the cooling period.

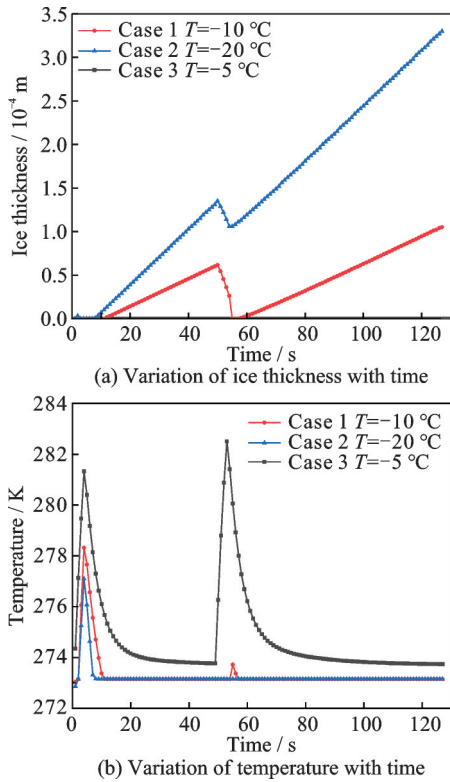


Fig.15 Results of the influence of temperature on ice thickness and surface temperature for Heater 2

Three temperature conditions of Heater 4 are discussed. As shown in Fig.16, the three cases at this location use heating control law 1, and the heat load of 4 W/cm² can remove the surface ice. The operation of adjacent heaters can raise the temperature of Heater 4 to 0 °C in Case 2. Comparing the temperature curves, it is observed that the lower the ambient temperature, the greater the rate of temperature

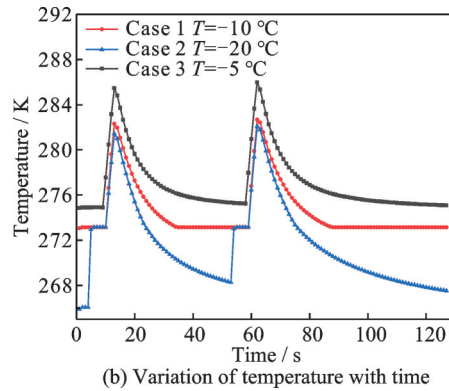
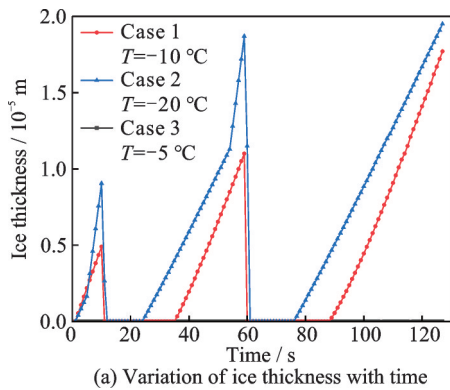


Fig.16 Results of influence of temperature on ice thickness and surface temperature for Heater 4

drop after the heating ends. In three cases, the temperature rising rates caused by the heating flux are similar.

4.2 Analysis of heating control laws at different ambient temperatures

Based on the analysis in the previous section, Case 3 exhibits energy waste. To reduce energy consumption, a strategy of decreasing the heater power is adopted for optimization. For Case 2, optimization is achieved by altering the electro-thermal control law. The atmospheric and icing conditions of the two optimized calculation cases are summarized in Table 6, referred to as Cases 4 and 5, respectively. The application of electro-thermal de-icing strategies must ensure that the duration of the surface temperature below the freezing point is not excessively long, thereby to guarantee the effectiveness of de-icing. It is also desirable to prevent the maximum surface temperature from becoming too high, to avoid the backward flow and freezing of runback water, which could lead to the formation of ice ridges. The optimization of electro-thermal control strategies aims to achieve reduced energy consumption.

In Case 4, the heater power density for all heating zones is 1.5 W/cm². In Case 5, Heater 2 uses 3 W/cm², while the remaining heaters use 2.5 W/cm². The heating control law 2 is shown in Fig.17.

Table 6 New calculation conditions

Case	Pressure/Pa	AOA/(°)	$V_{\infty}/(m \cdot s^{-1})$	$t_{\infty}/^{\circ}C$	MVD/ μm	LWC/($g \cdot m^{-3}$)	Control law
4	57 208	1.11	178.84	-5	25	0.3	1
5	57 208	1.11	178.84	-20	25	0.3	2

Heating control law 2 (233 s)										
Heater 1										14
Heater 2	14					14				
Heater 3		13					13			
Heater 4			11					11		
Heater 5				11						
Turn off					63					69
	14	27	38	49	112	126	139	150	164	233

Fig.17 Schematic diagram of heating control law 2

Case 4 calculates the condition where the heater power density is reduced to 1.5 W/cm^2 at the temperature of $-5 \text{ }^\circ\text{C}$. The results show that the surface temperature in the protected zone exceeds $0 \text{ }^\circ\text{C}$ for a short period, allowing some ice accretion, which is completely removed after heating begins. Fig.18 compares the temperature changes over de-icing cycle for Heater 2 in Cases 3 and 4. It is found that after reducing the heater power density to 1.5 W/cm^2 , the maximum temperature decreases from 280.5 K to 277.3 K , and the duration of the surface temperature above $0 \text{ }^\circ\text{C}$ is shortened by 78%. Although ice accumulates on the surface, the maximum ice thickness is only 0.0425 cm ; after heating began, the surface temperature quickly rises above $0 \text{ }^\circ\text{C}$, then the ice is rapidly removed, demonstrating good de-icing effectiveness.

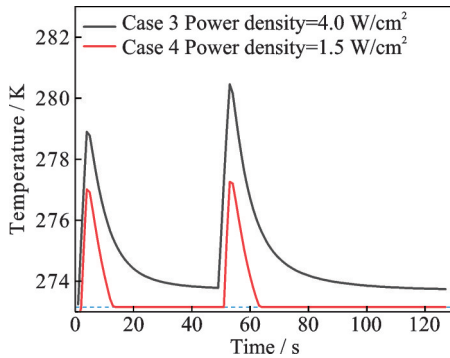


Fig.18 Analysis of Heater 2 for Cases 3 and 4

The energy consumption for each condition is calculated as

$$E_c = \int_t \int_s Q \, ds dt \quad (14)$$

$$e_c = E_c / t_{\text{cycle}} \quad (15)$$

where Q is the heater power density, and t_{cycle} the cycle time of heating control law.

The energy consumption E_c for Case 3 is calculated to be 1209 J , while for Case 4, it is 453 J , showing a 62% reduction in the overall system energy consumption. By employing the strategy of alter-

ing the heater power density, the duration for which the surface temperature exceeds $0 \text{ }^\circ\text{C}$ is shortened, and the required heating energy is also optimized, all while maintaining the de-icing effectiveness.

In the initial heating strategy Case 2, heating zones utilize a heater power density of 4 W/cm^2 , which meets the de-icing requirements for most areas. However, in the region where Heater 2 is located, there is incomplete ice removal. Under this circumstance, the method of changing the heater power density is not effective for optimization and leads to increased energy consumption instead. Therefore, the method of altering the heating control law is adopted for optimization.

A comparative analysis between Case 5 and Case 2 is conducted. Heating cycle 1 has a calculation time of 127 s , while heating cycle 2 has a calculation time of 233 s . Heating control law 2 increases both the heating time and the cooling time compared to control law 1, with an increased ratio of heating time to cooling time. The ice thickness-simulation time at the location of Heater 2 is illustrated in Fig.19, which clearly shows that using control law 2 effectively removes ice accretion, reduces ice thickness during the cooling phase, and overall provides better de-icing performance. Calculating the energy consumption, e_c for Case 2 is 9.52 W , and for Case 5, it is 9.56 W . With minimal change in energy consumption, the electro-thermal de-icing effectiveness is optimized.

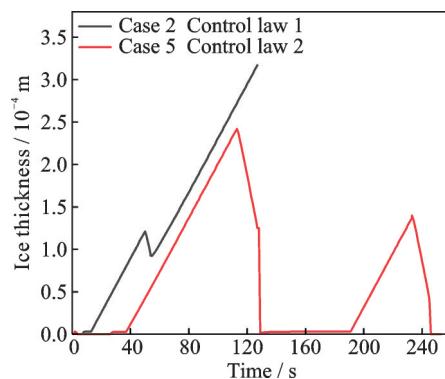


Fig.19 Analysis of Heater 2 for Cases 2 and 5

5 Conclusions

Flight safety is significantly impacted by air-

craft icing phenomena, and ice protection has been the subject of much domestic and international study. This study performs an unsteady simulation of the entire electro-thermal ice accretion-melting-deicing process by constructing the ice shedding model and taking into account the shedding behavior of the ice layer during the heating process. The electro-thermal de-icing properties of airfoil under multiple operating conditions are calculated, leading to the following conclusions.

(1) By combining ice accretion, melting, and ice shedding, this study develops a thorough mathematical model and computation technique for the electro-thermal de-icing process. When the ice shedding model is introduced, the ice in the protection region melts and sheds due to structural heat transfer, which results in a 28% reduction in ice mass when compared to simulations without the shedding model. This highlights how crucial the ice shedding model is for forecasting de-icing times and researching effective electro-thermal de-icing techniques.

(2) The duration of surface temperature above 0 °C is reduced by 78% after the strategy is optimized by lowering the heater power density for the scenario with an ambient temperature of -5 °C. Additionally, the system's overall energy usage can be reduced by 62% by fully removing the ice accretes that form throughout the cooling time. For the condition with the ambient temperature of -20 °C, optimizing the strategy by increasing the heating time improves the probability of ice shedding during the heating period and reduces ice thickness during the cooling period, thereby enhancing the electro-thermal de-icing effect while maintaining similar energy consumption.

(3) The electro-thermal de-icing control law can be considered from the following two aspects: (a) The duration of the de-icing surface temperature being below the freezing point should not be too long to ensure de-icing effectiveness; (b) the maximum surface temperature should not be too high to prevent the formation of excessively thick ice ridges in the overflow zone. At lower ambient temperatures, the de-icing cycle should be adjusted by in-

creasing the ratio of heating time to cooling time, balancing the de-icing effectiveness and energy consumption. At higher ambient temperatures, energy consumption can be optimized by reducing the heater power density.

To further explore the mechanisms of aircraft icing protection and optimize the design of icing protection systems, many issues remain to be studied. This paper simplifies the establishment of the ice shedding model, and mechanical characteristics of ice formed by water droplet impingement are not thoroughly analyzed. Incorporating experimental data to determine a more realistic shedding model will be the focus of future research.

References

- [1] SHEN X, WANG H, LIN G, et al. Unsteady simulation of aircraft electro-thermal de-icing process with temperature-based method[J]. Proceedings of the Institution of Mechanical Engineers, Part G: Journal of Aerospace Engineering, 2020, 234(2): 388-400.
- [2] CHAUVIN R, VILLEDIEU P, TRONTIN P, et al. A robust coupling algorithm applied to thermal ice protection system unsteady modeling[C]//Proceedings of the 6th AIAA Atmospheric and Space Environments Conference. Atlanta, USA: AIAA, 2014.
- [3] REID T, BARUZZI G S, ALIAGA C, et al. FENSAP-ICE: Application of unsteady CHT to de-icing simulations on a wing with inter-cycle ice formation[J]. AIAA Paper, 2010, 7835: 2010.
- [4] POURBAGIAN M, HABASHI W G. CFD-based optimization of electro-thermal wing ice protection systems in de-icing mode[C]//Proceedings of the 51st AIAA Aerospace Sciences Meeting Including the New Horizons Forum and Aerospace Exposition. Grapevine, USA: AIAA, 2013: 654.
- [5] POURBAGIAN M, HABASHI W G. Aero-thermal optimization of in-flight electro-thermal ice protection systems in transient de-icing mode[J]. International Journal of Heat and Fluid Flow, 2015, 54: 167-182.
- [6] HENRY R. Development of an electrothermal de-icing anti-icing model[C]//Proceedings of AIAA 30th Aerospace Sciences Meeting and Exhibi. Reno, USA: AIAA, 1992.
- [7] BENNANI L, VILLDIEU P, SALAUN M, et al. Numerical simulation and modeling of ice shedding: Process initiation[J]. Computers and Structures, 2014, 142: 15-27.

- [8] DING L, CHANG S N, YI X, et al. Coupled thermo-mechanical analysis of stresses generated in impact ice during in-flight de-icing[J]. *Applied Thermal Engineering*, 2020, 181: 115681.
- [9] KINTEA D M, ROISMAN I V, TROPEA C. Transport processes in a wet granular ice layer: Model for ice accretion and shedding[J]. *International Journal of Heat and Mass Transfer*, 2016, 97: 461-472.
- [10] SENGUPTA B, RAJ L P, CHO M Y, et al. Computational simulation of ice accretion and shedding trajectory of a rotorcraft in forward flight with strong rotor wakes[J]. *Aerospace Science and Technology*, 2021, 119: 107140.
- [11] ANTHONY J, HABASHI W B. Helicopter rotor ice shedding and trajectory analyses in forward flight[J]. *Journal of Aircraft*, 2021, 58(5): 1051-1067.
- [12] MORELLI M, GUARDONE A. A simulation framework for rotorcraft ice accretion and shedding[J]. *Aerospace Science and Technology*, 2022, 129: 107157.
- [13] WALLISCH J, HANN R. UAV icing: Experimental investigation of ice shedding times with an electrothermal de-icing system[C]//*Proceedings of AIAA Aviation 2022 Forum*. Chicago, USA: AIAA, 2022.
- [14] ENACHE A, BERNAY B, GLABEKE G, et al. Electrothermal ice protection systems de-icing: An experimentally validated idealized ice shedding model[J]. *AIAA Journal*, 2023, 61(6): 2526-2550.
- [15] WRIGHT W B. User manual for the NASA glenn ice accretion code LEWICE Version 2.2.2: NASA/CR—2002-211793[R]. Ohio: AIAA, 2002.
- [16] BIDWELL C. Ice Particle transport analysis with phase change for the E3 turbofan engine using LEWICE3D Version 3.2: NASA/TM—2012-217700[R]. Ohio: AIAA, 2012.
- [17] FOULADI H, HABASHI W B. FENSAP-ICE modeling of ice accretion on a helicopter fuselage in forward flight[C]//*Proceedings of the 4th AIAA Atmosphere and Space Environments Conference*. New Orleans, USA: AIAA, 2012.
- [18] DAVID S, HABASHI W G. FENSAP-ICE simulation of complex wind turbine icing events, and comparison to observed performance data[C]//*Proceedings of the 32nd ASME Wind Energy Symposium*. National Harbor, USA: AIAA, 2014.
- [19] BENNANI L, VILLDIEU P, SALAUN M. Two-dimensional model of an electro-thermal ice protection system[C]//*Proceedings of the 5th AIAA Atmosphere and Space Environments Conference*. San Diego, USA: AIAA, 2013.
- [20] AI Jianbo, DENG Jinghui, LIU Dajing. De-icing structure design of helicopter rotor blade[J]. *Helicopter Technique*, 2005(2): 12-15. (in Chinese)
- [21] BU Xueqin, LIN Guiping, YU Jia. Coupled heat transfer calculation on an airfoil electrothermal anti-icing surface[J]. *Journal of Aerospace Power*, 2010, 23(7): 1491-1496. (in Chinese)
- [22] CHANG Shinan, AI Suxiao, HUO Xiheng, et al. Improved simulation of electrothermal de-icing system[J]. *Journal of Aerospace Power*, 2008, 23(10): 1753-1758. (in Chinese)
- [23] LI Hai. Research on helicopter rotor blade electro-thermal de-icing technology[D]. Beijing: Beihang University, 2008. (in Chinese)
- [24] FU Jianping, ZHUANG Weiliang, YANG Bo, et al. Simulation of heating control law of electro-thermal de-icing of helicopter rotor blade[J]. *Journal of Beijing University of Aeronautics and Astronautics*, 2014, 40(9): 1200-1207. (in Chinese)
- [25] MU Zuodong. Study on aircraft icing and electro-thermal de-icing process[D]. Beijing: Beihang University 2018. (in Chinese)
- [26] RAUSA A, DONIZETTI A, GUARDONE A. Multi-physics simulation of 3D in-flight ice-shedding[J]. *Journal of Computational and Applied Mathematics*, 2023, 432: 115226.
- [27] RÖNNEBERG S, LAFORTE C, VOLAT C, et al. The effect of ice type on ice adhesion[J]. *AIP Advances*, 2019, 9(5): 055304.
- [28] FU Liang. Mechanism research of ice adhesion on aero-engine rotating components[D]. Shanghai: Shanghai Jiao Tong University 2016. (in Chinese)
- [29] SCAVUZZO R J, CHU M L, KELLACKEY C J. Impact ice stresses in rotating airfoils[J]. *Journal of Aircraft*, 1991, 28(7): 417-480.
- [30] LAFORTE J, PHAN L, FELIN B, et al. Microstructure of ice accretions grown on aluminum conductors[J]. *Journal of Applied Meteorology and Climatology*, 1983, 22(7): 1175-1189.
- [31] LIU Zonghui, BU Xueqin, LIN Guiping, et al. Simulation of unsteady electrothermal de-icing process based on PHengLEI[J]. *Acta Aerodynamica Sinica*, 2023, 41(2): 53-63. (in Chinese)
- [32] SHEN X, LIN G, YU J, et al. Three-dimensional numerical simulation of ice accretion at the engine inlet[J]. *Journal of Aircraft*, 2013, 50(2): 635-642.
- [33] AI-KHALILK K, HORVATH C, MILLER D, et al. Validation of NASA thermal ice protection comput-

er codes. III —The validation of ANTICE[C]//Proceedings of the 35th Aerospace Science Meeting. Reno, NV: AIAA, 1997.

Acknowledgement This research was supported by the National Natural Science Foundation of China (No. 52272428).

Authors

The first author Ms. ZHANG Yingying is the postgraduate student in school of Aeronautic Science and Engineering, Beihang University, Beijing, China. Her research has focused on aircraft icing and anti-icing technology.

The corresponding author Dr. BU Xueqin received the doctor degree from Beihang University in 2010. She has been engaged in the research of aircraft icing and anti-icing problems for many years, with good research results in 3D water droplet impact characteristics, internal and external

heat transfer coupling of hot air anti-icing system, design of hot air anti-icing system, 3D surface icing simulation, complex jet flow heat transfer, ice crystal icing, etc. She has received funding from Natural Science Foundation, National Key R&D Program, Aviation Foundation, etc.

Author contributions Ms. ZHANG Yingying performed simulation calculations, conducted the analysis and wrote the manuscript. Dr. BU Xueqin designed the models and revised the manuscript. Mr. YUAN Xiansheng contributed to the discussion and background of the study. Mr. XIONG Jingjiang processed some simulation data and conducted the analysis. All authors commented on the manuscript draft and approved the submission.

Competing interests The authors declare no competing interests.

(Production Editor: WANG Jing)

考虑冰脱落的电热除冰模型与仿真分析

张盈盈¹, 袁先圣², 熊荆江², 卜雪琴¹

(1. 北京航空航天大学航空科学与工程学院, 北京 100191, 中国;

2. 中国航发湖南动力机械研究所, 株洲 412002, 中国)

摘要: 电热防/除冰系统具有加热效率高、结构较为简单的特点, 是未来结冰防护的重要发展方向。现有电热除冰仿真算法对考虑冰脱落的结冰-融冰-除冰完整模型研究较少, 冰层在加热过程中融化脱离行为需要深入的研究和探讨。本文对冰脱落现象进行物理建模, 引入冰层在加热过程中的脱落行为, 改进现有电热除冰计算数学模型, 建立了电热除冰系统结冰-融冰-除冰模型, 开展了考虑冰脱落的电热除冰数值仿真、验证及优化分析。通过针对某机翼模型的多工况除冰数值模拟, 发现环境温度可以作为电加热防除冰策略环境适应性调整的因素。对计算工况机翼除冰控制率进行了加热热流密度与加热时间/冷却时间的优化。本文提出的改进的电热除冰模型和算法为电热除冰系统的设计提供了有力的技术支持。

关键词: 飞机结冰; 电热除冰; 冰脱落; 电加热控制律; 数值模拟